This is a preprint, the final version is subject to change, of the American Mineralogist (MSA)
Cite as Authors (Year) Title. American Mineralogist, in press.
DOI: https://doi.org/10.2138/am-2018-6395

Revision 2

Polyphase solid-inclusions formed by interactions between infiltrating fluids and precursor minerals enclosed in garnet of UHP rocks from the Dabie Shan, China

PENGLEI LIU[1,2,*], JUNFENG ZHANG[1], HANS-JOACHIM MASSONNE[2], AND ZHENMIN JIN[1]

[1]State Key Laboratory of Geological Processes and Mineral Resources, School of Earth Sciences, China University of Geosciences, 430074 Wuhan, China

[2]Institut für Mineralogie und Kristallchemie, Universität Stuttgart, Azenbergstr. 18, D-70174 Stuttgart, Germany

*Corresponding author. E-mail: liupengleiincug@aliyun.com

This is a preprint, the final version is subject to change, of the American Mineralogist (MSA)
Cite as Authors (Year) Title. American Mineralogist, in press.
DOI: https://doi.org/10.2138/am-2018-6395

ABSTRACT

Three types of polyphase solid-inclusions (PSIs) with distinct mineral assemblages and microstructures were found in garnet of an ultrahigh-pressure (UHP) eclogite-vein system from the Dabie Shan, east-central China. Type-1 PSI contains variable volumes of quartz, K-feldspar, plagioclase ± other phases, whereas type-2 PSI contains variable volumes of quartz, calcite ± other phases. Both types display shapes that are compatible with those of euhedral coesite inclusions. Type-3 PSI always contains a rutile core that is surrounded by plagioclase ± quartz and generally displays the morphology of the rutile core. Variable amounts of K-feldspar are embedded within the plagioclase of type-3 PSIs. The three PSI types developed fluid-mediated microstructures which include wedge-like offshoot and protrusion textures and inclusion-garnet interfaces controlled by the crystallographic structure of garnet. PSIs in peak minerals of UHP rocks have been previously thought to represent primary supercritical fluid or melt inclusions. Here we propose that the studied PSIs were formed under high-pressure (HP) eclogite-facies conditions during exhumation and represent reaction products between an enclosed mineral, such as coesite and rutile, and external fluids infiltrating the host garnet along fractures that have been healed later on. Two immiscible aqueous fluids (i.e., a siliceous and a carbonaceous) were involved in the formation of these PSIs. The siliceous fluid was rich in various large ion lithophile elements like Cs, Rb, Ba, K, Pb, Li, and Sr, whereas the carbonaceous fluid was rich in Pb and Sr. The new PSI formation mechanism proposed in this study bears significant implications for tracing fluid evolution and post-entrapment modifications of mineral inclusions in HP and UHP metamorphic rocks.

38 **Keywords:** Dabie Shan, ultrahigh-pressure, coesite, polyphase solid-inclusion, fluid-rock
39 interaction

40

INTRODUCTION

Ultrahigh-pressure (UHP) metamorphic rocks represent relicts of deeply-subducted crust and provide a natural laboratory to study the nature and behavior of metamorphic fluids in deep-seated subduction zones. The knowledge of the interaction of these fluids is important for understanding the formation, preservation, rheology and exhumation of UHP rocks and the possible mass transfer in subduction zones (e.g., Proyer, 2003; Zhang et al., 2004; Massonne, 2009; Labrousse et al., 2011; Zheng et al., 2011; Hermann et al., 2013; Frezzotti and Ferrando, 2015). However, there are considerable difficulties to characterize these fluids at present. One big obstacle is that the metamorphic fluids in deep-seated subduction zones usually escape from their site of interaction and leave little traces of their activity in natural rocks. Whereas experimental and theoretical studies are crucial for deciphering the physical and chemical properties of fluids in deep-seated subduction zones (e.g., Zheng et al., 2011; Hermann et al., 2013; Hermann and Rubatto, 2014), polyphase solid-inclusions (PSIs) in peak minerals such as garnet have been considered in the past two decades to be a good window for peering into UHP rocks affected by fluid interaction. Such inclusions commonly display an intergrowth of several daughter minerals, negative crystal shapes and wedge-like offshoots, and are interpreted to represent precursor supercritical fluid or melt inclusions (e.g., Hwang et al., 2001; Stöckhert et al., 2001, 2009; Ferrando et al., 2005; Korsakov and Hermann, 2006; Malaspina et al., 2006; Frezzotti et al., 2007; Frezzotti and Ferrando, 2015). Similar PSIs (known as nanogranitoids), crystallized from felsic melt, have been also reported in anatectic rocks of different crustal levels (e.g., Cesare et al., 2009, 2015; Ferrero et al., 2012, 2015; Bartoli et al., 2013). In all the reported cases, PSIs were normally considered

64 primary, i.e. they were captured during growth of the host phases.

65 Among the reported PSIs in UHP rocks, one group, mainly composed of quartz,
66 K-feldspar and/or plagioclase, has attracted substantial attention. The petrogenesis of this
67 group of PSI has been highly debated in the literature. Such PSIs have been interpreted as
68 the reaction products between coesite inclusions and a K-bearing omphacite host (Yang et
69 al., 1998), although their occurrence in garnet cannot be interpreted in the same way.
70 Another opinion refers to the former presence of composite K-cymrite + coesite
71 inclusions (Massonne, 2001; Massonne and Nasdala, 2003; Song et al., 2003; Zhang et al.,
72 2009), but it cannot account for the occurrence of larger quantities of plagioclase and/or
73 other minerals within such PSIs. In the light of recent studies, which suggest that these
74 PSIs could represent entrapped melts (e.g., Zeng et al., 2009; Gao et al., 2012, 2013, 2017;
75 Liu et al., 2013; Chen et al., 2014), we present here new perspectives on the formation of
76 quartz-feldspar-bearing PSIs in UHP rocks based on microstructural observations and a
77 geochemical study on their counterparts in garnet of an eclogite-vein system from the
78 Dabie UHP terrane, eastern China. Unlike primary PSIs, we demonstrate unequivocally
79 that these PSIs represent reaction products between precursor minerals (coesite and rutile)
80 in the inclusions and external fluids infiltrating the host garnet along fractures that have
81 been healed later on. Instead of melts, two immiscible aqueous fluids (i.e., a siliceous and
82 a carbonaceous) are proposed to have been involved in the formation of the investigated
83 PSIs.

84

85 **SAMPLE LOCATION AND ANALYTICAL METHODS**

86 The studied sample GJL12-4, collected from the Ganjialing area (N 30°38.666′, E

116°19.619′) in the Dabie UHP terrane, east-central China, is a decimeter-sized loose boulder of eclogite hosting centimeter-sized quartz-garnet veins (Fig. 1A, B). This boulder coexists with impure marbles in the field but the contact relationship is unclear. Former studies of the impure marbles have led to the discovery of coesite inclusions in dolomite and the derivation of peak P-T conditions of 4.2 ± 0.3 GPa and 745 ± 65 ^{o}C (Liu et al., 2015). In addition, intergranular coesite has been found in a metasedimentary rock from the same outcrop (Liu et al., 2017a). Descriptions of the geological background and regional geology of this outcrop can be found in Liu et al. (2015, 2017b).

The petrography of sample GJL12-4 was examined on thin sections using an optical microscope and a FEI Quanta 450 FEG scanning electron microscope (SEM) at the State Key Laboratory of Geological Processes and Mineral Resources (GPMR), China University of Geosciences (CUG), Wuhan. The SEM is equipped with an Oxford INCA X-Max 50 energy dispersive X-ray (EDX) spectrometer, which was used to identify tiny minerals and to map PSIs. The working conditions were 20 kV accelerating voltage, 5-6 μm spot size, and 12-15 mm working distance.

The major element chemistry of minerals was measured using a JEOL JXA-8100RL electron microprobe (EMP) with four wavelength dispersive X-ray (WDX) spectrometers and an EDX spectrometer at the GPMR. An accelerating voltage of 15 kV and a beam current of 20 nA were applied. A beam diameter between 1 and 5 μm was selected depending on the character of the analyzed mineral and its size. The counting times were 10 s for Na, K, Mg, Ca and Al, 20 s for Cr, Ti, Fe and Si, 15 s for Mn, and 30 s for Ba at peak and background. The ZAF method was used for data correction. Natural and synthetic silicates and oxides were used as standards. X-ray maps of selected garnet

grains containing PSIs were obtained in WDX mode using a CAMECA SX100 EMP at the Institut für Mineralogie und Kristallchemie, Universität Stuttgart. An accelerating voltage of 15 kV, a beam current of 50 nA, a step size of 2-3 μm, and a dwell time of 100 ms were applied.

The trace element chemistry of garnet and PSIs was analyzed in-situ on thin sections by a laser ablation inductively-coupled mass spectrometer (LA-ICP-MS) at the GPMR. Laser sampling was performed with a GeoLas 2005 system. The laser beam size, frequency and energy were set to 44 (for garnet) or 60 μm (for PSIs), 6 Hz and 70 mJ, respectively. An Agilent 7500a ICP-MS was used to determine ion-signal intensities. Helium (He) was used as the carrier gas and mixed with Argon (Ar) through a T-connector before entering the ICP. Nitrogen was imported into the central gas flow (Ar + He) of the Ar plasma to improve the detection limits and precision. For each analysis, the Agilent Chemstation was used to incorporate a background acquisition of 20-25 s and a subsequent 50 s acquisition for the sample. Off-line selection and integration of background and analytical signals, time-drift correction and quantitative calibration were performed by the software ICPMSDataCal (Liu et al., 2008). Element concentrations were calibrated against multiple reference materials BIR-1G, BCR-2G and BHVO-2G without using an internal standard (Liu et al., 2008).

SAMPLE DESCRIPTIONS

Both the eclogite and the quartz-garnet veins display a fine- to medium-grained texture (Fig. 1C-F). The eclogite partially preserved the peak mineral assemblage of garnet, phengite, coesite, dolomite, rutile, apatite (Fig. 1C, D), omphacite, and magnesite. Garnet

(ca. 40 vol%), occurring as anhedral to subhedral grains (0.1-1.5 mm), contains inclusions of coesite (Fig. 1C), omphacite, rutile, apatite, and zircon. Omphacite in the matrix has been totally replaced by amphibole + plagioclase symplectites (Fig. 1C). Phengite is often partially replaced by plagioclase + quartz pools that embed biotite clusters (Fig. 1D). Xenoblasts and coronae (around garnet, phengite, and dolomite) of amphibole and epidote are additional retrograde products. Dolomite (ca. 5-10 vol%) constitutes an important rock-forming mineral (Fig. 1C), whereas magnesite only occurs as an accessory phase.

The quartz-garnet veins display a sharp contact to the host eclogite (Fig. 1A, B). At their boundaries, amphibole + plagioclase symplectites in the eclogite are texturally preserved, without evidence of interaction with the veins. The veins comprise mainly garnet (ca. 40-45 vol%), quartz (ca. 40-45 vol%), and plagioclase (ca. 5-7 vol%) (Fig. 1E). Minor and accessory mineral phases are amphibole, epidote, apatite, phengite, K-feldspar, chlorite, calcite, rutile, ilmenite, titanite, sulfide, and zircon. Garnet (0.1-1.8 mm) in the veins displays a similar texture to that in the eclogite. It is partially replaced by amphibole or epidote in places and contains inclusions of quartz, rutile, apatite, and zircon. Plagioclase occurs as thin films or wide bands along the grain boundaries of garnet, quartz (Fig. 1F), apatite, and rutile, which grade into irregular pools in places (Fig. 1E). Relict coesite and polycrystalline quartz aggregates typically replacing coesite were not found in the vein garnet, but the prismatic and platy morphologies of some quartz inclusions (Fig. 2A, B) still suggest that they inherit their shapes from former coesite. The quartz inclusions display specific microstructures like wedge-like offshoot and protrusion textures and inclusion-garnet interfaces controlled by the crystallographic structure of

156 garnet (Fig. 2). In addition, small garnet blebs can be rarely found in quartz inclusions
157 (Fig. 2D).
158
159 **PSIS IN GARNET**
160 PSIs are common in the vein garnet. A single garnet grain generally contains one to
161 several PSIs that are distributed within this host mineral in a random way. The PSIs can
162 be subdivided into three major types (1, 2, and 3) on the basis of their mineral
163 assemblages and microstructures (Table 1). Type-1 PSIs comprise mainly variable
164 volumes of quartz and feldspar (Fig. 3A-K). Amphibole, epidote, titanite, ilmenite, calcite,
165 chlorite, and pyrite also occur within type-1 PSIs, but their occurrence and contents vary
166 considerably in these inclusions. Three subtypes were defined for type-1 PSIs (Table 1),
167 which are those containing quartz + K-feldspar ± other accessory phases (Type-1A: Fig.
168 3A-D), quartz + plagioclase ± other accessory phases (Type-1B: Fig. 3E-G) and two
169 feldspars ± other accessory phases (Type-1C: Fig. 3H-K). Type-2 PSIs (Fig. 3L) contain
170 variable volumes of quartz and calcite. In some of them chlorite, epidote, and/or titanite
171 form well-defined patches. Type-3 PSIs always contain a rutile core that is surrounded by
172 plagioclase ± quartz (Fig. 3M-P). Variable amounts of K-feldspar are embedded within
173 the plagioclase of type-3 PSIs. The rutile core is usually partially replaced by ilmenite ±
174 titanite (Fig. 3M-O). All PSIs contain oval microcavities (Fig. 3C, G, I, L-P) that could
175 represent exposed fluid inclusions. Type-1 and type-2 display regular or irregular shapes
176 and sizes from 5 × 20 μm to 200 × 300 μm. The regular ones are generally prismatic or
177 platy (Fig. 3A, C-E, H, J). Both regular and irregular types developed wedge-like
178 offshoot and protrusion textures (Fig. 3A-D, K, L) with serrated and straight

garnet-inclusion interfaces (Fig. 3B, C, G, I, L). Type-3 PSIs vary in size with diameters from tens of μm to more than 200 μm. Their general morphology is always similar to that of the rutile core (Fig. 3M-P). Type-3 PSIs developed a protrusion texture as well (Fig. 3O). Their interfaces with the host garnet are controlled by the crystallographic structure of garnet, as indicated by the angles between some interfaces (Fig. 3M-P). Although this feature is rare, it can be still traced for some type-1 and type-2 PSIs (Fig. 3F, I, L). It should be noted that BSE-brighter vein-like domains occur around the PSIs in garnet (Fig. 3E, F, K, L). These domains are cut by extant fractures that are locally sealed by chlorite (Fig. 3Q).

Garnet in the eclogite contains rare type-1 and type-2 PSIs similar to those in the vein garnet (Fig. 3Q-S). Type-3 PSIs are common in the eclogite but hardly contain K-feldspar (Fig. 3T). Given that PSIs in the veins are much more abundant and representative, we will focus on the PSIs in the veins hereafter unless specifically stated.

EDX mapping were performed on some PSIs in the eclogite-vein system, which reveal more details on the mineral assemblages in the PSIs (Fig. 4). For instance, some mineral phases (e.g., plagioclase and quartz) in single PSIs have a similar color in back scattered electron (BSE) images but they can be easily distinguished by EDX mapping (Fig. 4).

COMPOSITIONS OF GARNET AND PSIS

WDX mapping reveals that the rim of garnet in the eclogite-vein system experienced fluid-mediated alteration because, among others, this garnet domain (zone B) displays a completely different composition compared to the unaltered garnet (zone A), where the PSIs are generally included (Fig. 5). Garnet alteration texturally related to the occurrence

of the PSIs was not observed (Fig. 5). Regardless of the altered domain, garnet in the eclogite and in the veins is nearly compositionally homogeneous (Fig. 5). This mineral in the eclogite contains 44-50 mol% almandine, 32-39 mol% grossular, 14-18 mol% pyrope, and 1-2 mol% spessartine and shows a very similar composition to that in the veins: 43-50 mol% almandine, 32-41 mol% grossular, 12-17 mol% pyrope, and 1-2 mol% spessartine (Table 2). Also the trace element contents in both garnets are nearly identical. When normalized against chondrite and primitive mantle, the rare-earth element (REE) patterns and spider diagrams of garnet are characterized by enrichment of middle and heavy REEs (MREEs and HREEs) and Y and depletion of light REEs (LREEs) and large-ion lithophile elements (LILEs: Cs, Rb, Ba, K, Pb, Li, and Sr; Table 3; Figs. 6A and 7A).

Representative major-element chemistry of minerals constituting the PSIs is listed in Table 2. Both feldspars display a wide compositional range. The composition of plagioclase is $Ab_{73-100}An_{0-27}$. The K-feldspar can contain high BaO (0.85-14.5 wt%) but little Na_2O (0.19-1.22 wt%) and CaO (≤ 0.21 wt%) contents. According to the nomenclature of Leake et al. (1997), the amphibole can be classified as pargasite and tschermakite. This mineral contains 2.17-2.64 Al per formula unit (pfu) with Mg/(Mg + Fe^{2+}) ratios between 0.51 and 0.61. Only one spot analysis was obtained for epidote which contains 30 mol% pistacite. Chlorite shows a Mg/(Mg + Fe) ratio of 0.38. Titanite hosts 0.08-0.14 Al pfu. Calcite is nearly pure $CaCO_3$.

Only type-1 and type-2 PSIs were analyzed for their trace element chemistry. The used laser-beam size of 60 μm could cover the bulk inclusion in most selected cases. For several large PSIs, only a representative portion that contains all the inclusion phases was

sampled. As shown later, this will not influence our explanations or change our conclusions. Moreover, variable volumes of garnet ≤ 50 vol% were sampled together with the PSIs. In total, thirteen type-1 PSIs (+ garnet) were analyzed (Table 4). Compared with the host garnet, the mixtures commonly exhibit a prominent increase of the contents of LILEs (Fig. 7A). Since these elements are negligible in garnet, they could be assigned to the PSIs. The mixtures also exhibit various increase of the contents of LREE and high field-strength elements (HFSEs: Th, U, Nb, Ta, Ti; Table 4; Figs. 6A and 7A), which principally depend on the occurrence of some specific minerals within the PSIs. For example, the occurrence of epidote and titanite could cause the increase of the contents of LREE-Th-U and Nb-Ta-Ti, respectively (Table 4; Fig. 7A). In one case, the analyzed mixture displayed a remarkable increase of the contents of MREE-HREE-Y (Table 4; Figs. 6A and 7A) because the PSI contained Y-rich epidote proven by EDX analysis (Fig. 3C). In another case, high Zr and Hf contents were detected that could be related to micro-zircon beneath the thin section surface (Table 4; Fig. 7A).

In order to obtain the bulk compositions of pure type-1 PSIs, chemical contributions of garnet to the mixtures were subtracted based on the mean composition of the unaltered garnet domains in the veins and estimated garnet volumes incorporated into single analyses (Tables 4 and 5). Nevertheless, such estimations are semi-quantitative and involve large uncertainties. The distribution patterns of the calculated trace element compositions are always similar to those of the mixtures (Figs. 6 and 7). They exhibit a nearly flat MREE-HREE distribution with LREE depletion, LILE enrichment and $U_N > Th_N$ (Figs. 6B and 7B). Negative Nb-Ta-Ti and Zr-Hf anomalies were usually observed unless titanite and/or zircon were ablated (Fig. 7B).

Two large type-2 PSIs were partially analyzed without garnet (Table 4). As calcite and quartz distribute evenly within these two PSIs, the analytical results are supposed to be representative for the bulk inclusions. Compared to type-1 PSIs, these two type-2 PSIs contain much lower contents of trace elements except Pb and Sr (Table 5; Figs. 6B and 7B). Their REE patterns are similar to those of type-1 PSIs (Fig. 6B). In the spider diagrams, they display positive Pb and Sr anomalies with the contents of most other LILEs and HFSEs below the primitive mantle values and/or the detection limits (Fig. 7B).

GENERAL ASPECTS RELATED TO THE FORMATION OF THE ECLOGITE-VEIN SYSTEM

Garnet in the eclogite contains coesite inclusions (Fig. 1C), suggesting that the eclogite experienced UHP metamorphism. Applying conventional geothermobarometry, Liu et al. (2015) constructed a P-T path for the impure marbles that coexist with the eclogite-vein system. This P-T path is characterized by peak P-T conditions of 4.2 ± 0.3 GPa and 745 ± 65 ^{o}C that were followed by a nearly isothermal exhumation before late amphibolite-facies overprint. Preliminary work on the eclogite P-T evolution points to a similar P-T path but with somewhat lower peak P-T conditions ($P \geq 3.7$ GPa; T around 700 ^{o}C; Fig. 8).

Petrographic features described above suggest that the quartz-garnet veins within the eclogite formed by fluid infiltration during exhumation. The corresponding fluid-rock interactions should have proceeded along fractures that had developed in the eclogite (Fig. 1B). Three different fluid-mediated processes could have been responsible for the

formation of the quartz-garnet veins, which include: (1) circulated fluids directly precipitating new minerals in the open fractures; (2) flux melting (i.e. a melting process which involves infiltration of external water and other volatile components into a solid rock) of the original eclogite within the fracture zones; and (3) leaching of the original eclogite by passing fluids along the fracture zones. Garnet in the veins contains the same mineral (e.g., coesite) inclusions as that in the eclogite (Figs. 1C and 2A, B), and often displays a resorption texture along its rim. In addition, both garnets share virtually the same major and trace element chemistry (Tables 2 and 3; Figs. 6A and 7A). These features indicate that garnet in the veins is an original mineral from the eclogite instead of a newly-precipitated mineral. Thus, process (1) is not supported by evidence. The texture of amphibole + plagioclase symplectites in the eclogite is not disturbed by the quartz-garnet veins at the eclogite-vein boundaries indicating that the veins were formed at an eclogite-facies stage before the amphibolite-facies overprint. Extensive occurrence of plagioclase in the quartz-garnet veins (Fig. 1E, F) further constrains the formation of the veins at lower pressures than those at the reaction curve of albite = jadeite + quartz. Corresponding to such a late metamorphic stage, the retrograde P-T paths constructed for the eclogite and surrounding marble could have overstepped the wet solidus of a common eclogite (Fig. 8). However, a high degree of melting is required to remove a significant quantity of the original omphacite (and dolomite) in the fracture zones to produce a garnet-rich vein. Thus, the relatively low temperature around 650 °C leaves a significant water influx (i.e., a high water/rock ratio) as the only choice to comprehend the formation of quartz-garnet veins in the eclogite. In such a case, a dissolution-dominated leaching process should have played a dominant role in forming these veins instead of partial

melting. If the P-T path has never overstepped the wet solidus of a common eclogite, a dissolution-dominated leaching process can be the only candidate as formation mechanism for the veins.

According to the above considerations the quartz-garnet veins formed as follows: (1) fractures were opened in the host eclogite during early exhumation; (2) external aqueous fluids were introduced under eclogite-facies conditions, leading to a local high water/rock ratio in and near the fracture zones; (3) omphacite, dolomite ± other minerals in these zones were dissolved in the fluids which then precipitated new plagioclase and net quartz; (4) garnet in the fractures zones survived the dissolution process and were enriched in the leached zones to finally form the quartz-garnet veins.

A NEW MODEL FOR THE FORMATION OF PSIS

PSIs in this study display wedge-like offshoot and protrusion textures and inclusion-garnet interfaces controlled by the crystallographic structure of garnet (Fig. 3). These microstructures are similar to those of primary PSIs found in UHP (e.g., Stöckhert et al., 2001, 2009; Ferrando et al., 2005; Korsakov and Hermann, 2006; Frezzotti et al., 2007; Frezzotti and Ferrando, 2015) and anatectic rocks (e.g., Cesare et al., 2009, 2015; Ferrero et al., 2012, 2015; Bartoli et al., 2013), which could be best explained by fluid-mediated shape maturation and decrepitation of fluid-bearing inclusions within garnet (e.g., Roedder, 1984; Perchuk et al., 2005; Ferrero et al., 2012). Nevertheless, the investigated PSIs differ from the previous primary ones in several aspects. Primary PSIs are formed by entrapment of a fluid phase in a growing garnet and, thus, usually share the following features: (1) occurrence of inclusions in clusters in a specific domain of garnet;

317 (2) display of a constant polycrystalline mineral assemblage and (3) of a negative crystal
318 shape (an isometric shape with rhombododecahedral geometry). To be compared, PSIs in
319 this study are distributed randomly in garnet and a single garnet grain only contains one
320 (Fig. 1F) to several of them. In addition, the kind of the constituting minerals and their
321 proportions vary considerably in our PSIs (Fig. 3). Even though some inclusion-garnet
322 interfaces reflect the crystallographic control of the host mineral, PSIs in this study show
323 a typical negative crystal shape rarely (Fig. 3). Therefore, a formation mechanism
324 different to that of the primary PSIs is indicated for the investigated PSIs.

325 Type-1 and type-2 PSIs sometimes display a prismatic or a platy shape (Fig. 3A, C-E,
326 H, J, R), which is compatible with that of euhedral coesite inclusions. This leads us to
327 believe that external fluids could have infiltrated the host garnet along its fractures and
328 reacted with the precursor coesite inclusions, thereby inheriting their shapes. Such an
329 explanation is validated by the microstructures of type-3 PSIs (Fig. 3M-P, T). The rutile
330 (± ilmenite ± titanite) core within these PSIs is too large to be a daughter mineral
331 precipitated from an entrapped fluid. The rutile core is surrounded by feldspars ± quartz
332 and the whole inclusion always exhibits the general morphology of the rutile core. These
333 features suggest that a single rutile grain was once enclosed in garnet and external fluids
334 infiltrated this inclusion along the rutile-garnet interfaces. In response to this infiltration,
335 material was dissolved from the host garnet and/or the rutile core to enlarge the space for
336 accommodating the newly-precipitated feldspars ± quartz. Whether this process was
337 accompanied by the partial replacement of rutile by ilmenite and titanite must be called in
338 question. As outlined above, the fluid infiltration occurred still at conditions of the
339 eclogite-facies. At such conditions, rutile is the stable Ti-mineral, but local equilibria

leading to the formation of ilmenite and/or titanite already in the eclogite-facies cannot be ruled out. Concerning PSIs without typical coesite morphologies or rutile cores, the former presence of other mineral inclusions (e.g., omphacite and phengite; see Fig. 8 in Gao et al., 2014) is possible. The extant fractures in garnet could have served as the infiltration pathways for the fluids into the former mineral inclusions. If this was the case, some of these fractures should have been filled by minerals (such as feldspar) which are also present in the PSIs, not by chlorite which formed during very late alteration (Fig. 3Q). Therefore, the possibility of fluids infiltrating along the extant fractures can be ruled out. BSE-brighter vein-like domains occur around the PSIs in garnet (Fig. 3E, F, K, L), which are explained to represent early fractures that were healed during fluid-garnet interactions. In our opinion these early fractures are to be considered as the pathways for the fluid infiltration.

A detailed model on the formation of the studied PSIs is shown in Fig. 8. Coesite, rutile, and other metamorphic minerals were captured by growing garnet during prograde metamorphism (before stage A). During early decompression (from stage A to B), early fractures were created in garnet because of hydrofracturing and/or differential expansion of mineral inclusions relative to the host garnet (see Whitney, 1996). At stage B when the quartz-garnet veins were formed, aqueous fluids infiltrated the mineral inclusions along the early fractures and interacted with them and the host garnet via a dissolution-reprecipitation mechanism. As a microstructural response, the inclusion-garnet interfaces were adjusted to reduce the surface free energy (Roedder, 1984), resulting in straight, serrate, and smooth inclusion walls. Later decrepitation could lead to wedge-like offshoot and/or protrusion textures. The external fluid-mineral

363 inclusion-host garnet interaction continued until the amphibolite-facies stage C was
364 reached. The early fractures had been healed and our two representative PSIs were
365 formed. It should be noted that some monophase quartz inclusions after coesite display
366 microstructures reflecting a similar fluid-mediated process (Fig. 2). These quartz
367 inclusions and type-1 PSIs are interpreted to represent a continuous product series by
368 interaction between the precursor coesite inclusions and the infiltrating fluids.
369 Monophase quartz inclusions were instead formed when no new mineral was precipitated
370 from this interaction.

371 Coupled to the variation of constituent minerals and their contents within the PSIs (Fig.
372 3), the bulk composition of the PSIs varies considerably even if we only consider type-1
373 PSIs (Figs. 6 and 7). Such variations can be hardly interpreted as the result of a primary
374 entrapment process but can be explained using our new model: (1) the former mineral
375 (e.g., coesite, omphacite, phengite) inclusions changed from one case to the other; (2)
376 infiltrating fluids reacted with the former mineral inclusions and host garnet to different
377 degrees; and (3) the fluid composition evolved with the fluid-rock interaction. As
378 discussed in the subsequent section, more than one type of fluid phase had been involved
379 in the PSI formation, which could have also contributed to such variations.

380

381 **NATURE OF FLUIDS INVOLVED IN THE PSI FORMATION**

382 Recent studies proposed that type-1 PSIs represent silicate melts derived from
383 dehydration melting of phengite and/or paragonite (e.g., Zeng et al., 2009; Gao et al.,
384 2012, 2013, 2017; Liu et al., 2013; Chen et al., 2014; Wang et al., 2016). In addition,
385 calcite in type-2 PSIs was considered to reflect partial melting of subducted carbonates

386 (Gao et al., 2014). Nevertheless, no good arguments were given in these studies why
387 these PSIs should represent melts instead of aqueous fluids except that a P-T path was
388 envisaged to cross the dehydration melting curve of phengite. As seen in Fig. 8, the
389 newly-constructed P-T path is just like earlier ones obtained for different UHP eclogites
390 from the Dabie Shan (e.g., Carswell and Zhang, 1999; Zhang et al., 2003; Rolfo et al.,
391 2004). These paths do hardly cross the dehydration melting curve of phengite. Instead of
392 flux melting, we propose that a dissolution-dominated leaching process played the key
393 role in forming the PSI-bearing veins. This means that aqueous fluids instead of melts
394 should have been formed and dominated the fluid phase in the veins. Compared with
395 silicate melts, aqueous fluids have much lower viscosities (Audétat and Keppler, 2004)
396 and could more easily infiltrate the former mineral inclusions along garnet fractures.
397 Silicate melts, if they were really present and have dominated the fluid phase responsible
398 for the formation of PSIs, should have been felsic. Type-3 PSIs should have, thus,
399 contained quartz as a common mineral that resulted from the melt crystallization (type-1
400 and type-2 PSIs cannot give an unambiguous indication in this situation). However, this
401 is not the case (Fig. 3M-P, T). Besides, dark and/or white mica are common
402 crystallization products of felsic melt inclusions (e.g., Cesare et al., 2009, 2015; Ferrero
403 et al., 2012, 2015; Bartoli et al., 2013), which are absent in the studied PSIs (Fig. 3; also
404 see Zeng et al., 2009; Gao et al., 2012, 2013, 2017; Liu et al., 2013; Chen et al., 2014).
405 K-feldspar within the studied PSIs contains up to 14.5 wt% BaO (Table 2). Such Ba-rich
406 K-feldspar has been also documented for similar PSIs in other studies (e.g., Yang et al.,
407 1998; Zeng et al., 2009; Gao et al., 2012; Liu et al., 2013; Chen et al., 2014; Wang et al.,
408 2016). It is noteworthy that the occurrence of Ba-rich K-feldspar is often reported to be

409 related to the activities of aqueous fluids (e.g., Harlov et al., 1998; Moro et al., 2001; Shi
410 et al., 2010; Henry et al., 2015). This relation is compatible with the fact that Ba is highly
411 compatible in aqueous fluids (e.g., Green and Adam, 2003; Kessel et al., 2005; Tsay et al.,
412 2017). Thus, Ba-rich K-feldspar within the studied PSIs provides another argument that
413 fluids involved in the formation of these PSIs were aqueous fluids instead of hydrous
414 melts.

415 Related to the fluid nature and the formation of type-3 PSIs, the efficiency of material
416 removal from the rutile inclusions and the host garnet (see above) must be considered. At
417 given P-T conditions, the solubility of Ti in aqueous fluids largely depends on the fluid
418 chemistry. For example, high F concentrations can significantly enhance the solubility of
419 Ti in aqueous fluids (e.g., Rapp et al., 2010). However, the efficiency of Ti removal from
420 the rutile inclusions by aqueous fluids depends not only on its solubility but also on time.
421 As long as the disequilibrium state was maintained between the infiltrating fluids and the
422 rutile inclusions while the garnet fractures stayed open, chemical gradients in the fluids
423 could lead to continuous removal of Ti from the rutile inclusions. This explanation can be
424 applied to the partial removal of garnet as well. Dissolution of rutile and garnet didn't
425 produce any new Ti- or FeMg-bearing mineral in type-3 PSIs probably because chemical
426 gradients in the fluids could not result in saturation of these elements at the dissolving site,
427 i.e. the dissolved elements of Ti-Fe-Mg would diffuse away from the dissolving site.

428 In the light of our new model described above, recovering the composition of the
429 interacting aqueous fluids through analyzing the bulk composition of the PSIs is nearly
430 impossible unless the bulk distribution coefficient of each element between such fluids
431 and the PSIs is known. Besides, we have to consider the possibility of disequilibrium

between the newly-precipitated minerals and the fluids. Nevertheless, we can still put some compositional constraints on the interacting aqueous fluids. Precipitation of feldspars in type-1 and type-3 PSIs indicate that the aqueous fluids were rich in Si-Al-Na-K components. Calcite in type-2 PSIs suggests that a second immiscible aqueous fluid rich in carbon could have been present. Regarding trace elements, Figs. 6 and 7 indicate that the siliceous aqueous fluids were rich in LILEs (Cs, Rb, Ba, K, Pb, Li, Sr) and that the carbonaceous fluids were rich in Pb and Sr. Such fluids were probably at a first stage generated in the subducting oceanic crust at great depths but relatively low temperatures and then infiltrated hotter rocks which were exhumed in a subduction channel (see Massonne, 2012; Liu et al., 2017b) such as the eclogite investigated here.

CONCLUDING REMARKS AND IMPLICATIONS

In this study a new model was proposed for the formation of PSIs, which has important implications for tracing fluid evolution and post-entrapment modifications of mineral inclusions (such as coesite) in high-pressure-UHP metamorphic rocks. This new model indicates that PSIs enclosed in peak minerals (particularly those showing fractures and/or healed fractures) of such rocks are not always primary as previously thought and that PSIs do not necessarily represent entrapped supercritical fluid or melt inclusions. In addition, we conclude that recovering the fluid composition through integrating the bulk composition of this kind of PSIs should be cautious (see Gao et al., 2012, 2013, 2014, 2017; Liu et al., 2013; Chen et al., 2014) though certain geochemical fingerprints can be qualitatively traced.

ACKNOWLEDGEMENTS

We thank S. Zheng (Wuhan) and T. Theye (Stuttgart) for assistance with the EMP and T. Luo (Wuhan) for help with the LA-ICP-MS analyses. This study was funded by grant from the National Key Basic Research Program of China (No.2015CB856101). Thorough reviews by S. Ferrero, I. Klonowska, and an anonymous reviewer as well as careful editorial handling by K. Ashley are gratefully acknowledged.

REFERENCES CITED

Audétat, A., and Keppler, H. (2004) Viscosity of fluids in subduction zones. Science, 303, 513-516.

Auzanneau, E., Vielzeuf, D., and Schmidt, M.W. (2006) Experimental evidence of decompression melting during exhumation of subducted continental crust. Contributions to Mineralogy and Petrology, 152, 125-148.

Bartoli, O., Cesare, B., Poli, S., Bodnar, R.J., Acosta-Vigil, A., Frezzotti, M.L., and Meli, S. (2013) Recovering the composition of melt and the fluid regime at the onset of crustal anatexis and S-type granite formation. Geology, 41, 115-118.

Bohlen, S.R., and Boettcher, A.L. (1982) The quartz-coesite transformation: a pressure determination and the effects of other components. Journal of Geophysical Research, 87, 7073-7078.

Bundy, F.P. (1980) The P, T phase and reaction diagram for elemental carbon. Journal of Geophysical Research, 87, 7073-7078.

Carswell, D.A., and Zhang, R.Y. (1999) Petrographic characteristics and metamorphic evolution of ultrahigh-pressure eclogites in plate-collision belts. International Geology Review, 41, 781-798.

Cesare, B., Ferrero, S., Salvioli-Mariani, E., Pedron, D., and Cavallo, A. (2009) "Nanogranite" and glassy inclusions: The anatectic melt in migmatites and granulites. Geology, 37, 627-630.

Cesare, B., Acosta-Vigil, A., Bartoli, O., and Ferrero, S. (2015) What can we learn from melt inclusions in migmatites and granulite? Lithos, 239, 186-216.

Chen Y.X., Zheng, Y.F., Gao, X.Y., and Hu, Z.C. (2014) Multiphase solid inclusions in

zoisite-bearing eclogite: evidence for partial melting of ultrahigh-pressure metamorphic rocks during continental collision. Lithos, 200-201, 1-21.

Ferrando, S., Frezzotti, M.L., Dallai, L., and Compagnoni, R. (2005) Multiphase solid inclusions in UHP rocks (Su-Lu, China): remnants of supercritical silicate-rich aqueous fluids released during continental subduction. Chemical Geology, 223, 68-81.

Ferrero, S., Bartoli, O., Cesare, B., Salvioli-Mariani, E., Acosta-Vigil, A., Cavallo, A., Groppo, C., and Battiston, S. (2012) Microstructures of melt inclusions in anatectic metasedimentary rocks. Journal of Metamorphic Geology, 30, 303-322.

Ferrero, S., Wunder, B., Walczak, K., O'Brien, R.J., and Ziemann, M.A. (2015) Preserved near ultrahigh-pressure melt from continental crust subducted to mantle depths. Geology, 43, 447-450.

Frezzotti, M.L., and Ferrando, S. (2015) The chemical behavior of fluids released during deep subduction based on fluid inclusions. American Mineralogist, 100, 352-377.

Frezzotti, M.L., Ferrando, S., Dallai, L., and Compagnoni, R. (2007) Intermediate alkali-alumino-silicate aqueous solutions released by deeply subducted continental crust: fluid evolution in UHP OH-rich topaz-kyanite quartzites from Donghai (Sulu, China). Journal of Petrology, 48, 1219-1241.

Gao, X.Y., Zheng, Y.F., and Chen Y.X. (2012) Dehydration melting of ultrahigh-pressure eclogite in the Dabie orogen: evidence from multiphase solid inclusions in garnet. Journal of Metamorphic Geology, 30, 193-212.

Gao, X.Y., Zheng, Y.F., Chen Y.X., and Hu, Z.C. (2013) Trace element composition of continentally subducted slab-derived melt: insight from multiphase solid inclusions in ultrahigh-pressure eclogite in the Dabie orogeny. Journal of Metamorphic Geology, 31,

453-468.

Gao, X.Y., Zheng, Y.F., Chen Y.X., and Hu, Z.C. (2014) Composite carbonate and silicate multiphase solid inclusions in metamorphic garnet from ultrahigh-P eclogite in the Dabie orogen. Journal of Metamorphic Geology, 32, 961-980.

Gao, X.Y., Chen, Y.X., and Zhang, Q.Q. (2017) Multiphase solid inclusions in ultrahigh-pressure metamorphic rocks: A snapshot of anatectic melts during continental collision. Journal of Asian Earth Sciences, 145, 192-204.

Green, T.H., and Adam, J. (2003) Experimentally-determined trace element characteristics of aqueous fluid from dehydrated mafic oceanic crust at 3.0 GPa, 650-700 °C. European Journal of Mineralogy, 15, 815-830.

Harlov, D.E., Hansen, E.C., and Bigler, C. (1998) Petrologic evidence for K-feldspar metasomatism in granulite facies rocks. Chemical Geology, 151, 373-386.

Henry, D.J., and Will, C.N. (2015) Ba-rich K-feldspar from mafic xenoliths within Mesoarchean granitic rocks, Beartooth Mountains, Montana, USA: indicators for barium metasomatism. The Canadian Mineralogist, 53, 185-198.

Hermann, J., and Rubatto, D. (2014) Subduction of continental crust to mantle depth: geochemistry of ultrahigh-pressure rocks. In H.D. Holland and K.K. Turekian, Treatise on Geochemistry, 2nd ed., vol 4, 309-340. Elsevier, Oxford.

Hermann, J., Zheng, Y.F., and Rubatto, D. (2013) Deep fluids in subducted continental crust. Elements, 9, 281-287.

Hwang, S.L., Shen, P.Y., Chu, H.T., Yui, T.F., and Lin, C.C. (2001). Genesis of microdiamonds from melt and associated multiphase inclusions in garnet of ultrahigh-pressure gneiss from Erzgebirge, Germany. Earth and Planetary Science

Letters, 188, 9-15.

Kessel, R., Schmidt, M.W., Ulmer, P., and Pettke, T. (2005) Trace element signature of subduction-zone fluids, melts and supercritical liquids at 120-180 km depth. Nature, 437, 724-727.

Korsakov, A.V., and Hermann, J. (2006) Silicate and carbonate melt inclusions associated with diamonds in deeply subducted carbonate rocks. Earth and Planetary Science Letters, 241, 104-118.

Labrousse, L., Prouteau, G., and Ganzhorn, A.C. (2011) Continental exhumation triggered by partial melting at ultrahigh pressure. Geology, 39, 1171-1174.

Lambert, I.B., and Wyllie, P.J. (1972) Melting of gabbro (quartz eclogite) with excess water to 35 kilobars, with geological applications. Journal of Geology, 80, 693-708.

Leake, B.E., Woolley, A.R., Arps, C.E.S., Birch, W.D., Gilbert, M.C., Grice, J.D., Hawthorne, F.C., Kato, A., Kisch, H.J., Krivovichev, V.G., Linthout, K., Laird, J., Mandarino, J., Maresch, W.V., Nickel, E.H., Schumaker, J.C., Smith, D.C., Stephenson, N.C.N., Ungaretti, L., Whittaker, E.J.W., and Guo, Y.Z. (1997) Nomenclature of amphiboles: report of the subcommittee on amphiboles of the International Mineralogical Association Commission on New Minerals and Mineral Names. American Mineralogist, 61, 295-321.

Li, X.P., Zheng, Y.F., Wu, Y.B., Chen, F.K., Gong, B., and Li, Y.L. (2004) Low-T eclogite in the Dabie terrane of China: petrological and isotopic constraints on fluid activity and radiometric dating. Contributions to Mineralogy and Petrology, 148, 443-470.

Liu, P.L., Wu, Y., Chen, Y., Zhang, J.F., and Jin, Z.M. (2015) UHP impure marbles from

554 the Dabie Mountains: metamorphic evolution and carbon cycling in continental
555 subduction zones. Lithos, 212-215, 280-297.
556 Liu, P.L., Massonne, H.-J., Zhang, J.F., Wu, Y., and Jin, Z.M. (2017a) Intergranular
557 coesite and coesite inclusions in dolomite from the Dabie Shan: constraints on the
558 preservation of coesite in UHP rocks. Terra Nova, 29, 154-161.
559 Liu, P.L., Massonne, H.-J., Wu, Y., Jin, Z.M., and Zhang, J.F. (2017b) Diopside, apatite,
560 and rutile in an ultrahigh pressure impure marble from the Dabie Shan, eastern China:
561 A record of eclogite-facies metasomatism during exhumation. Chemical Geology, 466,
562 123-139.
563 Liu, Q., Jin, Z.M., and Zhang, J.F. (2009) An experimental study of dehydration partial
564 melting of a phengite-bearing eclogite at 1.5-3.0 GPa. Chinese Science Bulletin, 54,
565 2090-2100.
566 Liu, Q., Hermann, J., and Zhang, J. (2013) Polyphase inclusions in the Shuanghe UHP
567 eclogites formed by subsolidus transformation and incipient melting during
568 exhumation of deeply subducted crust. Lithos, 177, 91-109.
569 Liu, Y.S., Hu, Z.C., Gao, S., Günther, D., Xu, J., Gao, C.G., and Chen, H.H. (2008) In
570 situ analysis of major and trace elements of anhydrous minerals by LA-ICP-MS
571 without applying an internal standard. Chemical Geology, 257, 34-43.
572 Malaspina, N., Hermann, J., Scambelluri, M., and Compagnoni, R. (2006) Polyphase
573 inclusions in garnet-orthopyroxenite (Dabie Shan, China) as monitors for
574 metasomatism and fluid-related trace element transfer in subduction zone peridotite.
575 Earth and Planetary Science Letters, 249, 173-187.
576 Massonne, H.-J. (2001) First find of coesite in the ultrahigh-pressure metamorphic area of

577 the central Erzgebirge, Germany. European Journal of Mineralogy, 13, 565-570.
578 Massonne, H.-J. (2009) Hydration, dehydration, and melting of metamorphosed granitic
579 and dioritic rocks at high- and ultrahigh-pressure conditions. Earth and Planetary
580 Science Letters, 288, 244-254.
581 Massonne, H.-J. (2012) Formation of amphibole and clinozoisite-epidote in eclogite
582 owing to fluid infiltration during exhumation in a subduction channel. Journal of
583 Petrology, 53, 1969-1998.
584 Massonne, H.-J., and Nasdala, L. (2003) Characterization of an early metamorphic stage
585 through inclusions in zircon of a diamondiferous quartzofeldspathic rock from the
586 Erzgebirge, Germany. American Mineralogist, 88, 883-889.
587 McDonough, W.F., and Sun, S.S. (1995) The composition of the Earth. Chemical
588 Geology, 120, 223-253.
589 Mibe, K., Kawamoto, T., Matsukage, K.N., Fei, Y.W., and Ono, S. (2011) Slab melting
590 versus slab dehydration in subduction-zone magmatism. Proceedings of the National
591 Academy of Sciences, 108, 8177-8182.
592 Moro, M.C., Cembranos, M.L., and Fernandez, A. (2001) Celsian, (Ba, K)-feldspar and
593 cymrite from sedex barite deposits of Zamora, Spain. The Canadian Mineralogist, 39,
594 1039-1051.
595 Perchuk, A.L., Burchard, M., Maresch, W.V., and Schertl, H.P. (2005) Fluid-mediated
596 modification of garnet interiors under ultrahigh-pressure conditions. Terra Nova, 17,
597 545-553.
598 Proyer, A. (2003). The preservation of high-pressure rocks during exhumation:
599 metagranites and metapelites. Lithos, 70, 183-194.

Rapp, J.F., Klemme, S., Butler, I.B., and Harley, S.L. (2010) Extremely high solubility of rutile in chloride and fluoride-bearing metamorphic fluids: An experimental investigation. Geology, 38, 323-326.

Roedder, E. (1984) Fluid Inclusions, Reviews in Mineralogy, 12, 678.

Rolfo, F., Compagnoni, R., Wu, W.P., and Xu, S.T. (2004) A coherent lithostratigraphic unit in the coesite-eclogite complex of Dabie Shan, China: geologic and petrologic evidence. Lithos, 73, 71-94.

Shi, G.H., Jiang, N., Wang, Y.W., Zhao, X., Wang, X., Li, G.W., EG, E., and Cui, W.Y. (2010) Ba minerals in clinopyroxene rocks from the Myanmar jadeitite area: implications for Ba recycling in subduction zones. European Journal of Mineralogy, 22, 199-214.

Song, S.G., Yang, J.S., Xu, Z.Q., Liou, J.G., and Shi, R.D. (2003) Metamorphic evolution of the coesite-bearing ultrahigh-pressure terrane in the North Qaidam, Northern Tibet, NW China. Journal of Metamorphic Geology, 21, 631-644.

Stöckhert, B., Duyster, J., Trepmann, C., and Massonne, H.-J. (2001) Microdiamond daughter crystals precipitated from supercritical COH + silicate fluids included in garnet, Erzgebirge, Germany. Geology, 29, 391-394.

Stöckhert, B., Trepmann, C., and Massonne, H.-J. (2009) Decrepitated UHP fluid inclusions: about diverse phase assemblages and extreme decompression rates (Erzgebirge, Germany). Journal of Metamorphic Geology, 27, 673-684.

Sun, S.S., and McDonough, W.F. (1989) Chemical and isotopic systematics of oceanic basalts: implications for mantle composition and processes. Geological Society Special Publication, 42, 313-345.

623 Tsay, A., Zajacz, Z., Ulmer, P., and Sanchez-Valle, C. (2017) Mobility of major and trace
624 elements in the eclogite-fluid system and element fluxes upon slab dehydration.
625 Geochimica et Cosmochimica Acta, 198, 70-91.
626 Wang, S.J., Wang, L., Brown, M., and Feng, P. (2016) Multi-stage barite crystallization in
627 partially melted UHP eclogite from the Sulu belt, China. American Mineralogist, 101,
628 564-579.
629 Whitney, D.L. (1996) Garnets as open systems during regional metamorphism. Geology,
630 24, 147-150.
631 Yang, J.J., Godard, G., and Smith, D.C. (1998) K-feldspar-bearing coesite pseudomorphs
632 in an eclogite from Lanshantou (Eastern China). European Journal of Mineralogy, 10,
633 969-985.
634 Zeng, L.S., Liang, F.H., Asimow, P., Chen, F.Y., and Chen, J. (2009) Partial melting of
635 deeply subducted continental crust and the formation of quartzofeldspathic polyphase
636 inclusions in the Sulu UHP eclogites. Chinese Science Bulletin, 54, 2580-2594.
637 Zhang, J.F., Green, H.W., Bozhilov, K., and Jin, Z.M. (2004) Faulting induced by
638 precipitation of water at grain boundaries in hot subducting oceanic crust. Nature, 428,
639 633-636.
640 Zhang, R.Y., Liou, J.G., Zheng, Y.F., and Fu, B. (2003) Transition of UHP eclogites to
641 gneissic rocks of low-amphibolite facies during exhumation: evidence from the Dabie
642 terrrane, central China. Lithos, 70, 269-291.
643 Zhang, R.Y., Liou, J.G., Iizuka, Y., and Yang, J.S. (2009) First record of K-cymrite in
644 North Qaidam UHP eclogite, Western China. American Mineralogist, 94, 222-228.
645 Zheng, Y.F., Xia, Q.X., Chen, R.X., and Gao, X.Y., (2011) Partial melting, fluid

646 supercriticality and element mobility in ultrahigh-pressure metamorphic rocks during
647 continental collision. Earth-Science Reviews, 107, 342-374.

648

FIGURE CAPTIONS

FIGURE 1. (A) Photograph and (B) scanned image of two sections cut from the eclogite-vein system (sample GJL12-4). The coin in (A) is 2 cm in diameter. (C-E) Photomicrographs and (F) mixed mapping image of eclogite (C, D) and quartz-garnet veins (E, F). Mineral abbreviations in this study: Ab-albite, Alm-almandine, Amp-amphibole, An-anorthite, And-andradite, Ap-apatite, Bt-biotite, Cal-calcite, Chl-chlorite, Cn-celsian, Coe-coesite, Dia-diamond, Dol-dolomite, Ep-epidote, Gra-graphite, Gro-grossular, Grt-garnet, Ilm-ilmenite, Jd-jadeite, Kfs-K-feldspar, Or-orthoclase, Phn-phengite, Pl-plagioclase, Prp-pyrope, Py-pyrite, Q-quartz, Ru-rutile, Sp-spessartine, Ttn-titanite, Zr-zircon.

FIGURE 2. BSE images of monophase quartz inclusions within garnet of quartz-garnet veins. Wedge-like offshoot (pink arrows) and protrusion (blue arrows) textures and inclusion-garnet interfaces controlled by the crystallographic structure of garnet (red lines) are indicated. Note that some quartz inclusions display a prismatic (A) or platy (B) shape.

FIGURE 3. BSE images of PSIs within garnet of quartz-garnet veins (A-P) and eclogite (Q-T). Three PSI types can be recognized: type-1 (A-K, Q, R), type-2 (L, S), and type-3 (M-P, T). See text in details. Healed fractures (black arrows), wedge-like offshoot (pink arrows) and protrusion (light blue arrows) textures, serrate inclusion-garnet interfaces (green arrows), possible crystal faces of garnet (dark blue arrows), and exposed fluid inclusions (red arrows) are indicated.

672 **FIGURE 4.** Mixed mapping images and single element mapping images of two PSIs
673 (EDX mode). See their BSE images in Fig. 3I and M, respectively.
674
675 **FIGURE 5.** Element mapping images of three garnet grains containing PSIs (WDX
676 mode). The garnet rim was altered by fluids with zone A and B representing the original
677 and the altered domains, respectively. Note that PSIs only occur in zone A and did not
678 cause any compositional alteration of garnet. In (D) and (G) are outlined the two garnet
679 grains containing PSIs, where in (A) is only shown part of a single PSI-bearing garnet
680 grain.
681
682 **FIGURE 6.** Chondrite-normalized REE patterns of garnet and PSIs: (A) unaltered garnet
683 and mixtures of type-1 PSI + unaltered garnet; (B) calculated type-1 and type-2 PSIs.
684 Chondrite values are from Sun and McDonnough (1989).
685
686 **FIGURE 7.** Primitive mantle-normalized spider diagrams of garnet and PSIs: (A)
687 unaltered garnet and mixtures of type-1 PSI + unaltered garnet; (B) calculated type-1 and
688 type-2 PSIs. Primitive mantle values are from McDonnough and Sun (1995).
689
690 **FIGURE 8.** Petrogenesis of PSIs in this study. Coesite and rutile were enclosed by
691 growing garnet during prograde metamorphism (before stage A). From stage A to B, early
692 fractures opened in garnet, along which external fluids infiltrated mineral inclusions.
693 Then, interactions between fluid, inclusion, and garnet were initiated and continued until
694 stage C. The early fractures (white lines) had been healed and two representative PSIs

were produced. New fractures (black lines) opened later on. C-1 and C-2 are the two PSIs at stage C, which are enlarged to highlight their microstructures. Wedge-like offshoot and protrusion textures and serrate inclusion-garnet interfaces are indicated by pink, light blue and green arrows, respectively. Phase-transition curves of diamond = graphite, coesite = quartz, and albite = jadeite + quartz are after Bundy (1980), Bohlen and Boettcher (1982), and Li et al. (2004), respectively. Curves 1 and 2 are the phengite-dehydration melting curves in metagreywacke (Auzanneau et al., 2006) and eclogite (Liu et al., 2009), respectively. Arrow lines are P-T paths constructed for the Dabie UHP eclogites: pink-this study, green-Carswell and Zhang (1999), grey-Zhang et al. (2003), and yellow-Rolfo et al. (2004). The blue line refers to the wet basalt solidus after Lambert and Wyllie (1972). The blue solid circle is the second critical point of basalt after Mibe et al. (2011).

This is a preprint, the final version is subject to change, of the American Mineralogist (MSA)
Cite as Authors (Year) Title. American Mineralogist, in press.
DOI: https://doi.org/10.2138/am-2018-6395

TABLE 1. Summary of mineral assemblages and microstructures of PSIs in the eclogite-vein system

PSI types	Mineral assemblages	Notes on mineral assemblages	Key microstructures
Type-1A	Quartz + K-feldspar ± accessory minerals	Accessory amphibole, epidote, titanite, ilmenite, calcite, chlorite, and pyrite occur in type-1 PSIs, but their occurrence and contents vary considerably.	Type-1 and -2 PSIs have similar microstructures: prismatic, platy, and irregular shapes; with wedge-like offshoot and protrusion textures; serrated and straight garnet-inclusion interfaces; surrounded by healed fractures.
Type-1B	Quartz + plagioclase ± accessory minerals		
Type-1C	Plagioclase + K-feldspar ± accessory minerals		
Type-2	Quartz + calcite	Chlorite, epidote, and/or titanite may form well-defined patches in some type-2 PSIs.	
Type-3	Rutile core + surrounding plagioclase ± K-feldspar	Rutile core is usually partially replaced by ilmenite ± titanite. Quartz was only found in one type-3 PSI.	With a general morphology of the rutile core and a protrusion texture; inclusion-garnet interfaces controlled by the crystallographic structure of garnet; surrounded by healed fractures.

This is a preprint, the final version is subject to change, of the American Mineralogist (MSA)
Cite as Authors (Year) Title. American Mineralogist, in press.
DOI: https://doi.org/10.2138/am-2018-6395

TABLE 2. Major element compositions (wt%) of selected minerals in the eclogite-vein system

Rock	Eclogite		Q-Grt vein														
Mineral	Grt		Grt		Amp		Chl		Ep	Pl		Kfs			Ttn		Cal
Texture	Unaltered		Unaltered		In PSI		In PSI		In PSI	In PSI		In PSI			In PSI		In PSI
Spot	16-15	16-19	13-6	13-55	13-21	13-99	13-14	13-17	13-19	13-20	13-97	13-16	13-30	13-50	13-15	13-88	13-27
SiO_2	38.51	38.07	38.85	38.41	44.09	40.85	27.64	27.58	39.00	67.95	60.41	63.00	60.43	51.69	32.46	37.48	-
Al_2O_3	21.63	21.32	21.19	21.14	12.57	14.75	17.68	17.41	22.25	19.83	24.60	18.41	19.58	21.91	6.06	3.47	-
TiO_2	0.08	0.11	0.14	0.15	0.25	0.88	0.02	0.04	0.06	0.03	0.04	0.11	0.50	0.59	31.70	31.89	-
MgO	4.07	3.59	4.07	4.03	9.81	8.30	11.05	11.11	0.09	0.01	0.09	0.00	0.01	0.03	0.18	0.04	0.02
CaO	12.55	14.50	14.10	14.14	10.50	11.06	0.09	0.22	22.14	0.47	5.56	0.05	0.07	0.08	27.98	26.00	55.51
FeO	22.83	21.01	21.04	21.21	17.79	18.38	31.49	31.94	13.30	0.25	0.48	0.48	0.42	0.62	0.76	0.68	0.58
Cr_2O_3	0.05	0.00	0.00	0.00	0.00	0.01	0.01	0.00	0.00	0.00	0.00	0.00	0.00	0.00	0.00	0.00	-
MnO	0.46	0.45	0.54	0.50	0.04	0.07	0.18	0.17	0.06	0.00	0.00	0.00	0.00	0.01	0.00	0.00	0.05
Na_2O	0.06	0.06	0.01	0.02	2.38	2.31	0.13	0.10	0.00	11.31	8.04	0.29	0.29	0.53	0.01	0.00	-
K_2O	0.00	0.00	0.00	0.00	0.24	0.95	0.02	0.02	0.01	0.02	0.35	15.19	14.02	9.70	0.07	0.00	-
BaO	-	-	-	-	-	-	-	-	-	-	-	2.15	4.99	14.53	-	-	-
Total	100.25	99.10	99.94	99.60	97.67	97.56	88.31	88.58	96.90	99.86	99.57	99.68	100.31	99.68	99.22	99.58	56.16
O	12.00	12.00	12.00	12.00	23.00	23.00	14.00	14.00	25.00	8.00	8.00	8.00	8.00	8.00	3.00	3.00	1.00
Si	2.98	2.97	3.02	2.98	6.47	6.12	2.98	2.98	6.39	2.98	2.70	2.97	2.88	2.65	0.63	0.71	-
Al	1.97	1.96	1.94	1.94	2.17	2.61	2.25	2.21	4.30	1.02	1.30	1.02	1.10	1.33	0.14	0.08	-
Ti	0.00	0.01	0.01	0.01	0.03	0.10	0.00	0.00	0.01	0.00	0.00	0.00	0.02	0.02	0.46	0.46	-
Mg	0.47	0.42	0.47	0.47	2.15	1.85	1.78	1.79	0.02	0.00	0.01	0.00	0.00	0.00	0.01	0.00	0.00
Ca	1.04	1.21	1.17	1.18	1.65	1.78	0.01	0.03	3.89	0.02	0.27	0.00	0.00	0.00	0.58	0.53	0.99
Fe^{3+}	0.02	0.03	0.05	0.06	0.81	0.54	-	-	1.82	-	-	-	-	-	-	-	-
Fe^{2+}	1.46	1.34	1.32	1.32	1.37	1.77	2.84	2.88	-	0.01	0.02	0.02	0.02	0.03	0.01	0.01	0.01
Cr	0.00	0.00	0.00	0.00	0.00	0.00	0.00	0.00	0.00	0.00	0.00	0.00	0.00	0.00	0.00	0.00	-
Mn	0.03	0.03	0.04	0.03	0.00	0.01	0.02	0.02	0.01	0.00	0.00	0.00	0.00	0.00	0.00	0.00	0.00
Na	0.01	0.01	0.00	0.00	0.68	0.67	0.03	0.02	0.00	0.96	0.70	0.03	0.03	0.05	0.00	0.00	-
K	0.00	0.00	0.00	0.00	0.04	0.18	0.00	0.00	0.00	0.00	0.02	0.91	0.85	0.64	0.00	0.00	-
Ba	-	-	-	-	-	-	-	-	-	-	-	0.04	0.09	0.28	-	-	-
Total	7.99	7.98	8.02	7.99	15.37	15.63	9.91	9.93	16.45	4.99	5.01	4.99	4.99	5.01	1.84	1.79	1.00
Mg#	0.24	0.24	0.26	0.26	0.61	0.51	0.38	0.38	-	-	-	-	-	-	-	-	-
Alm	0.49	0.45	0.44	0.44	-	-	-	-	Ab	0.98	0.71	0.03	0.03	0.05	-	-	-
Gro	0.34	0.39	0.37	0.36	-	-	-	-	An	0.02	0.27	0.00	0.00	0.00	-	-	-
Prp	0.16	0.14	0.16	0.16	-	-	-	-	Or	0.00	0.02	0.93	0.88	0.65	-	-	-
And	0.01	0.02	0.03	0.03	-	-	-	-	Cn	-	-	0.04	0.09	0.29	-	-	-
Sp	0.01	0.01	0.01	0.01	-	-	-	-	-	-	-	-	-	-	-	-	-

"-" = undetected or uncalculated. Ferric contents are calculated as follows: garnet = 5 six- and eight-fold coordinated cations; Amp = total cations - Ca - Na - K = 13; Ep = total Fe. Mg# = $Mg/(Mg+Fe^{2+})$.

This is a preprint, the final version is subject to change, of the American Mineralogist (MSA)
Cite as Authors (Year) Title. American Mineralogist, in press.
DOI: https://doi.org/10.2138/am-2018-6395

TABLE 3. Trace element compositions (ppm) of unaltered garnet domains in the eclogite-vein system

Rock	Spot	Li	Be	B	P	K	Sc	Ti	V	Cr	Co	Ni	Cu	Zn	Ga	Rb	Sr	Y	Zr	Nb	Cs
Eclogite	1	bdl	0.25	0.16	199	2.85	97.2	275	150	31.8	19.2	0.41	0.40	91.5	14.8	bdl	0.058	152	1.16	0.29	bdl
	2	0.21	0.67	bdl	190	bdl	94.2	316	158	59.7	18.7	bdl	bdl	96.5	14.4	0.14	bdl	154	0.56	0.15	bdl
Q-Grt vein	1	0.44	bdl	3.29	94.6	bdl	58.7	583	108	29.6	23.3	1.27	0.23	77.2	14.3	2.67	0.19	121	2.04	bdl	0.080
	2	0.47	0.012	3.17	96.8	bdl	58.8	671	150	66.6	24.6	1.19	0.038	78.9	14.8	0.060	0.11	105	2.35	bdl	bdl
	3	0.068	bdl	3.60	107	0.047	71.9	623	129	43.1	21.9	1.26	0.29	81.1	14.2	bdl	0.14	141	3.17	bdl	bdl
	4	0.19	0.027	3.61	97.9	bdl	65.7	408	126	36.4	27.2	1.27	0.11	85.1	13.3	0.007	0.089	156	1.92	0.003	bdl
	5	0.15	bdl	4.11	105	bdl	59.5	677	146	59.3	23.4	0.93	0.14	78.0	14.3	0.005	0.092	107	2.31	0.007	0.006
	6	bdl	0.057	4.51	75.0	2.54	65.2	199	96.5	60.9	30.4	1.05	0.10	89.4	9.79	bdl	0.041	176	0.89	0.007	0.001

Continued

Rock	Spot	Ba	La	Ce	Pr	Nd	Sm	Eu	Gd	Tb	Dy	Ho	Er	Tm	Yb	Lu	Hf	Ta	Pb	Th	U
Eclogite	1	bdl	0.028	0.004	bdl	0.48	3.78	1.66	13.8	3.56	25.3	5.47	13.7	1.95	17.6	2.29	0.26	bdl	0.060	bdl	0.13
	2	bdl	0.078	bdl	0.11	1.79	5.24	1.75	14.2	3.82	24.6	5.25	15.0	1.97	17.1	2.25	0.34	0.038	0.056	0.12	0.11
Q-Grt vein	1	0.18	0.11	0.27	0.071	0.78	1.66	0.90	6.93	2.09	17.9	4.44	14.3	1.92	13.6	1.93	0.026	bdl	0.034	0.004	0.067
	2	bdl	0.020	0.055	0.052	0.64	1.24	0.72	4.70	1.56	14.4	3.72	12.3	1.89	11.3	1.79	0.041	0.003	0.084	0.009	0.038
	3	bdl	0.002	0.13	0.061	0.86	1.57	1.01	7.61	2.24	20.1	5.13	16.9	2.49	16.3	2.52	0.031	bdl	0.032	bdl	0.075
	4	bdl	0.009	0.14	0.081	1.25	2.87	1.69	10.1	2.94	24.8	5.53	18.5	2.40	16.2	2.32	0.042	bdl	0.054	0.011	0.14
	5	0.090	0.004	0.069	0.029	0.60	1.18	0.72	5.29	1.68	14.3	3.86	12.4	1.80	12.3	1.72	0.026	bdl	0.028	0.018	0.057
	6	bdl	0.006	0.032	0.011	0.69	2.56	2.02	14.0	3.65	28.6	6.42	19.7	2.66	16.9	2.68	bdl	0.003	0.10	0.010	0.035

"bdl" = below detection limit.

This is a preprint, the final version is subject to change, of the American Mineralogist (MSA)
Cite as Authors (Year) Title. American Mineralogist, in press.
DOI: https://doi.org/10.2138/am-2018-6395

TABLE 4. Trace element compositions (ppm) of polyphase solid inclusion ± garnet in the quartz-garnet veins

PSI types	Ablated minerals	Grt/vol%	Li	Be	B	P	K	Sc	Ti	V	Cr	Co	Ni	Cu	Zn	Ga	Rb	Sr	Y	Zr	Nb	Cs
Type-1A	Kfs+Chl+Q	30	7.27	bdl	3.46	182	16900	41.1	275	49.7	8.12	19.8	0.52	0.91	77.1	9.14	36.6	23.4	189	1.02	bdl	0.27
Type-1A	Q+Kfs+Chl+Y-Ep	25	5.71	21.4	531	299	1112	58.0	1351	100	2.63	18.6	0.87	1.88	75.9	13.1	3.36	2.00	3321	3.96	1.02	0.17
Type-1B	Q+Pl+Ep+Cal+***Zr***	10	0.99	0.057	40.0	143	699	62.5	1163	159	18.7	3.67	1.12	0.41	13.0	12.8	2.16	81.5	187	72.3	0.30	0.42
Type-1B	Amp+Pl+Ep	50	4.40	0.40	6.04	151	2749	82.2	1020	143	56.5	23.9	2.37	2.25	88.3	13.4	3.72	54.7	105	3.47	0.50	0.23
Type-1C	Pl+Kfs	50	0.99	0.050	3.55	235	113	77.9	729	137	59.1	19.2	1.92	0.75	77.2	14.0	0.42	0.55	113	2.65	0.036	0.018
Type-1C	Pl+Kfs	50	4.29	bdl	22.0	128	21029	45.1	458	37.6	4.28	13.4	0.91	1.27	60.3	10.8	89.7	209	118	1.14	0.26	0.91
Type-1C	Pl+Amp+Kfs	50	4.77	0.15	21.2	148	14503	73.5	840	127	31.7	20.4	1.31	1.18	82.5	10.9	55.0	157	110	1.08	0.15	1.02
Type-1C	Pl+Amp+Kfs	5	5.11	0.42	15.9	120	16423	93.4	1490	179	90.7	21.4	2.68	1.17	103	14.0	64.8	178	115	3.37	2.01	0.70
Type-1C	Kfs+Pl+Cal	50	2.33	0.13	6.87	112	23075	42.7	365	92.3	9.80	16.7	1.25	1.85	59.0	10.4	64.1	21.2	111	1.46	bdl	0.43
Type-1C	Ep+Pl+Kfs+Py	5	0.17	bdl	14.4	98.1	435	59.2	244	89.4	31.0	4.96	0.61	1.61	4.74	11.3	1.13	30.9	117	1.06	0.019	0.25
Type-1C	Pl+Amp+Kfs+Chl	50	11.8	0.20	4.70	175	9401	64.9	730	131	66.8	21.3	0.64	0.14	82.8	13.6	27.5	83.6	104	2.23	0.39	0.10
Type-1C	Pl+Amp+Chl+Kfs	50	1.48	bdl	2.66	225	1168	62.6	552	118	45.3	21.9	1.15	0.66	75.9	13.7	3.70	36.2	116	2.23	0.012	0.35
Type-1C	Kfs+Pl+Chl+Amp+***Ttn***	20	22.3	0.35	77.9	133	46167	29.8	18698	110	21.7	14.0	3.97	2.29	80.6	9.62	196	158	52.4	2.42	29.7	1.30
Type-2	Cal+Q	0	0.006	0.077	bdl	41.5	18.2	0.98	6.63	1.20	0.55	0.37	0.82	6.70	7.35	0.20	0.10	65.9	7.48	0.13	0.028	0.055
Type-2	Cal+Q	0	bdl	0.25	0.18	31.0	1.54	0.079	bdl	bdl	bdl	0.070	0.11	0.39	1.35	bdl	0.092	55.0	5.93	bdl	0.003	bdl

Continued

PSI types	Ablated PSI minerals	Grt/vol%	Ba	La	Ce	Pr	Nd	Sm	Eu	Gd	Tb	Dy	Ho	Er	Tm	Yb	Lu	Hf	Ta	Pb	Th	U
Type-1A	Kfs+Chl+Q	30	7554	0.29	0.34	0.075	1.12	2.74	1.57	15.1	3.78	30.5	7.12	22.2	2.88	21.1	3.08	0.007	0.040	0.38	0.017	0.045
Type-1A	Q+Kfs+Chl+Y-Ep	25	264	0.82	2.29	0.41	3.61	13.0	5.07	137	47.7	467	121	386	50.8	292	41.1	0.095	0.053	0.35	1.26	1.12
Type-1B	Q+Pl+Ep+Cal+***Zr***	10	282	3.58	4.79	0.43	2.38	2.58	1.70	12.7	3.32	28.8	6.61	21.1	2.73	19.5	3.10	1.66	0.021	7.51	0.53	0.56
Type-1B	Amp+Pl+Ep	50	241	0.23	0.57	0.11	1.14	1.40	0.83	7.09	2.08	18.3	3.90	12.0	1.49	9.92	1.48	0.057	0.022	1.31	0.040	0.025
Type-1C	Pl+Kfs	50	23.4	0.036	0.30	0.053	0.48	1.18	0.70	5.20	1.63	15.3	4.02	13.8	2.26	15.2	2.59	0.029	0.004	0.21	0.015	0.026
Type-1C	Pl+Kfs	50	4667	0.21	0.42	0.097	1.01	1.35	0.91	6.62	2.02	16.9	4.80	14.9	1.98	15.1	2.29	0.020	0.007	1.41	0.020	0.021
Type-1C	Pl+Amp+Kfs	50	5074	0.079	0.26	0.055	0.85	2.09	1.21	9.42	2.44	19.2	4.31	12.2	1.68	12.2	1.89	0.078	0.014	1.33	bdl	0.035
Type-1C	Pl+Amp+Kfs	5	5022	0.079	0.19	0.058	0.39	0.61	0.59	5.87	1.80	18.4	4.32	15.1	2.18	12.3	1.77	0.12	0.13	3.21	0.005	0.018
Type-1C	Kfs+Pl+Cal	50	5489	1.95	2.35	0.23	1.04	1.00	0.69	6.02	1.77	15.8	4.30	13.2	2.06	12.5	2.13	bdl	bdl	0.41	0.049	0.085
Type-1C	Ep+Pl+Kfs+Py	5	212	0.075	0.13	0.071	0.52	1.41	1.52	9.28	2.33	18.1	4.07	13.0	1.91	12.1	1.83	0.020	0.002	11.0	0.019	0.062
Type-1C	Pl+Amp+Kfs+Chl	50	6366	0.045	0.18	0.028	0.43	1.04	0.54	5.20	1.42	13.7	3.60	12.8	2.00	13.9	2.18	0.036	0.006	0.37	0.020	bdl
Type-1C	Pl+Amp+Chl+Kfs	50	602	0.017	0.12	0.071	1.02	1.22	0.94	5.56	1.87	17.2	4.06	13.1	1.97	15.0	2.37	0.052	0.006	0.43	0.009	0.083
Type-1C	Kfs+Pl+Chl+Amp+***Ttn***	20	22095	0.38	0.97	0.10	0.92	1.28	0.47	6.88	1.18	10.2	1.94	5.11	0.65	4.63	0.62	0.13	5.16	1.03	0.13	0.11
Type-2	Cal+Q	0	5.55	0.038	0.038	0.008	0.049	0.062	bdl	0.24	0.10	0.93	0.21	0.67	0.081	0.48	0.058	0.010	bdl	2.07	bdl	0.011
Type-2	Cal+Q	0	4.40	0.014	0.018	bdl	0.016	0.076	0.011	0.17	0.052	0.52	0.16	0.57	0.079	0.34	0.13	bdl	0.002	0.30	bdl	0.002

Ablated PSI minerals are given in the order of visual modal content. The minerals highlighted in italics are not observed on the thin section surface and their presence is inferred from the analytical results. "bdl" = below detection limit.

This is a preprint, the final version is subject to change, of the American Mineralogist (MSA)
Cite as Authors (Year) Title. American Mineralogist, in press.
DOI: https://doi.org/10.2138/am-2018-6395

TABLE 5. Calculated trace element compositions (ppm) of polyphase solid inclusions in the quartz-garnet veins

PSI types	Ablated PSI minerals	Li	Be	B	P	K	Sc	Ti	V	Cr	Co	Ni	Cu	Zn	Ga	Rb	Sr	Y	Zr	Nb	Cs
Type-1A	Kfs+Chl+Q	10.3	bdl	3.35	218	24142	31.6	167	17.2	bdl	17.6	0.25	1.23	75.2	7.31	52.0	33.4	212	0.55	bdl	0.37
Type-1A	Q+Kfs+Chl+Y-Ep	7.53	28.5	706	366	1483	56.2	1626	92.0	bdl	16.5	0.77	2.45	74.0	13.0	4.25	2.64	4383	4.58	1.35	0.22
Type-1B	Q+Pl+Ep+Cal+***Zr***	1.07	0.059	44.0	149	776	62.4	1233	163	15.2	1.28	1.12	0.44	5.41	12.7	2.32	90.5	193	80.1	0.33	0.46
Type-1B	Amp+Pl+Ep	8.53	0.77	8.36	206	5497	101	1513	160	63.7	22.7	3.58	4.34	95.1	13.4	6.76	109	76.3	4.82	1.00	0.43
Type-1C	Pl+Kfs	1.71	0.068	3.39	373	224	92.4	931	149	68.9	13.3	2.68	1.35	72.7	14.6	0.16	1.00	91.0	3.18	0.067	0.007
Type-1C	Pl+Kfs	8.32	bdl	40.3	161	42056	26.9	390	bdl	bdl	1.56	0.66	2.39	39.0	8.22	179	417	101	0.16	0.51	1.78
Type-1C	Pl+Amp+Kfs	9.27	0.26	38.8	201	29004	83.7	1154	128	14.0	15.7	1.46	2.21	83.3	8.45	109	315	85.1	0.037	0.29	2.01
Type-1C	Pl+Amp+Kfs	5.37	0.44	16.5	121	17288	94.9	1541	182	92.8	21.2	2.76	1.23	104	14.0	68.1	187	114	3.43	2.12	0.74
Type-1C	Kfs+Pl+Cal	4.40	0.23	10.0	128	46149	22.1	204	58.9	bdl	8.34	1.33	3.55	36.3	7.45	127	42.4	87.3	0.81	bdl	0.84
Type-1C	Ep+Pl+Kfs+Py	0.17	bdl	15.0	98.2	458	59.0	229	87.5	30.0	3.89	0.58	1.69	0.69	11.2	1.15	32.5	117	1.00	0.020	0.27
Type-1C	Pl+Amp+Kfs+Chl	23.2	0.37	5.68	253	18800	66.5	934	137	84.3	17.6	0.11	0.13	83.9	13.8	54.2	167	74.1	2.35	0.77	0.17
Type-1C	Pl+Amp+Chl+Kfs	2.70	bdl	1.60	355	2336	61.8	577	110	41.3	18.7	1.13	1.17	70.1	13.9	6.71	72.3	96.6	2.36	0.019	0.67
Type-1C	Kfs+Pl+Chl+Amp+***Ttn***	27.8	0.43	96.4	142	57709	21.4	23241	105	14.8	11.2	4.68	2.83	80.4	8.67	245	197	31.9	2.49	37.1	1.62
Type-2	Cal+Q	0.006	0.077	bdl	41.5	18.2	0.98	6.63	1.20	0.55	0.37	0.82	6.70	7.35	0.20	0.10	65.9	7.48	0.13	0.028	0.055
Type-2	Cal+Q	bdl	0.25	0.18	31.0	1.54	0.079	bdl	bdl	bdl	0.070	0.11	0.39	1.35	bdl	0.092	55.0	5.93	bdl	0.003	bdl

Continued

PSI types	Ablated PSI minerals	Ba	La	Ce	Pr	Nd	Sm	Eu	Gd	Tb	Dy	Ho	Er	Tm	Yb	Lu	Hf	Ta	Pb	Th	U
Type-1A	Kfs+Chl+Q	10792	0.40	0.44	0.086	1.26	3.13	1.74	18.1	4.38	35.0	8.09	25.0	3.18	23.9	3.47	bdl	0.056	0.52	0.020	0.035
Type-1A	Q+Kfs+Chl+Y-Ep	353	1.09	3.02	0.53	4.55	16.7	6.37	179	62.8	617	159	509	67.0	384	54.1	0.12	0.070	0.44	1.68	1.47
Type-1B	Q+Pl+Ep+Cal+***Zr***	313	3.97	5.31	0.47	2.56	2.66	1.76	13.2	3.43	29.8	6.81	21.7	2.79	20.1	3.21	1.84	0.023	8.34	0.58	0.62
Type-1B	Amp+Pl+Ep	481	0.44	1.03	0.17	1.47	0.95	0.49	6.08	1.79	16.5	2.95	8.29	0.78	5.39	0.80	0.080	0.042	2.56	0.071	bdl
Type-1C	Pl+Kfs	46.6	0.047	0.48	0.055	0.17	0.52	0.23	2.30	0.90	10.5	3.18	11.9	2.33	16.0	3.03	0.026	0.005	0.36	0.021	bdl
Type-1C	Pl+Kfs	9333	0.39	0.73	0.14	1.22	0.85	0.64	5.15	1.68	13.7	4.74	14.2	1.77	15.7	2.42	0.006	0.010	2.77	0.031	bdl
Type-1C	Pl+Amp+Kfs	10148	0.13	0.40	0.060	0.90	2.34	1.25	10.7	2.53	18.3	3.77	8.61	1.17	10.0	1.61	0.12	0.026	2.60	bdl	0.002
Type-1C	Pl+Amp+Kfs	5286	0.082	0.19	0.059	0.37	0.54	0.56	5.75	1.78	18.3	4.29	15.0	2.18	12.2	1.75	0.13	0.14	3.37	0.004	0.015
Type-1C	Kfs+Pl+Cal	10978	3.88	4.58	0.41	1.29	0.16	0.20	3.94	1.18	11.7	3.75	10.7	1.92	10.5	2.10	bdl	bdl	0.76	0.089	0.10
Type-1C	Ep+Pl+Kfs+Py	223	0.078	0.13	0.072	0.50	1.39	1.54	9.34	2.33	18.0	4.03	12.8	1.90	12.0	1.81	0.020	0.002	11.5	0.019	0.061
Type-1C	Pl+Amp+Kfs+Chl	12731	0.065	0.24	0.005	0.057	0.24	bdl	2.31	0.48	7.37	2.35	9.99	1.80	13.4	2.20	0.038	0.008	0.68	0.030	bdl
Type-1C	Pl+Amp+Chl+Kfs	1203	0.009	0.13	0.091	1.24	0.59	0.71	3.01	1.39	14.4	3.28	10.5	1.75	15.6	2.57	0.072	0.009	0.81	0.008	0.10
Type-1C	Kfs+Pl+Chl+Amp+***Ttn***	27619	0.47	1.18	0.11	0.95	1.14	0.30	6.57	0.88	7.73	1.21	2.46	0.26	2.18	0.24	0.15	6.45	1.28	0.16	0.12
Type-2	Cal+Q	5.55	0.038	0.038	0.008	0.049	0.062	bdl	0.24	0.10	0.93	0.21	0.67	0.081	0.48	0.058	0.010	bdl	2.07	bdl	0.011
Type-2	Cal+Q	4.40	0.014	0.018	bdl	0.016	0.076	0.011	0.17	0.052	0.52	0.16	0.57	0.079	0.34	0.13	bdl	0.002	0.30	bdl	0.002

Ablated PSI minerals are given in the order of visual modal content. The minerals highlighted in italics are not observed on the thin section surface and their presence is inferred from the analytical results. "bdl" = below detection limit.

This is a preprint, the final version is subject to change, of the American Mineralogist (MSA)
Cite as Authors (Year) Title. American Mineralogist, in press.
DOI: https://doi.org/10.2138/am-2018-6395

Figure 1

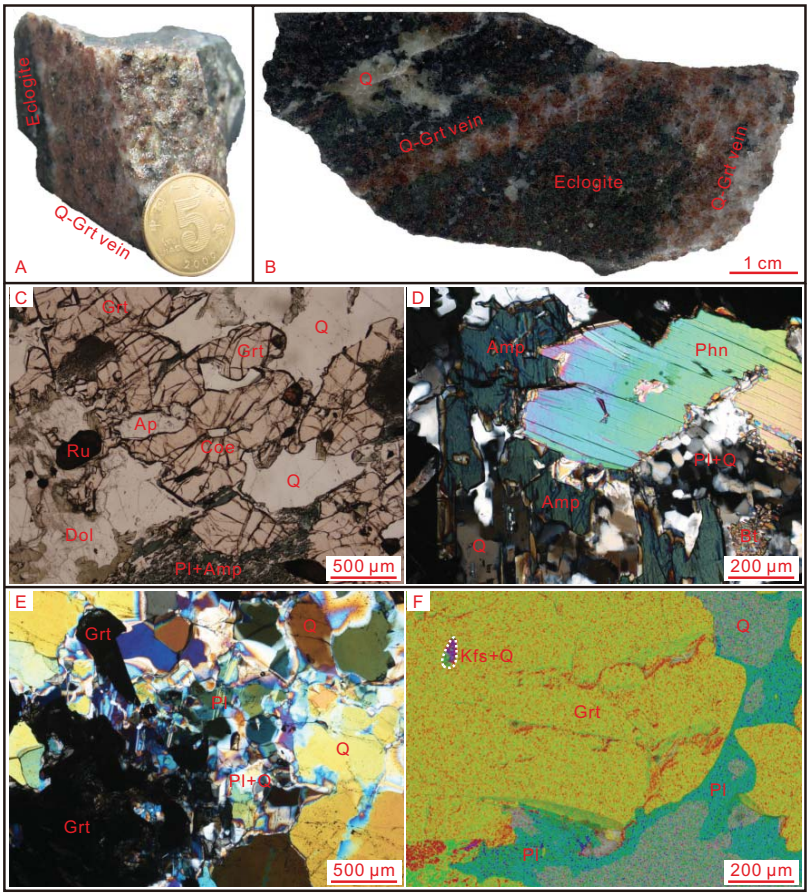

This is a preprint, the final version is subject to change, of the American Mineralogist (MSA)
Cite as Authors (Year) Title. American Mineralogist, in press.
DOI: https://doi.org/10.2138/am-2018-6395

Figure 2

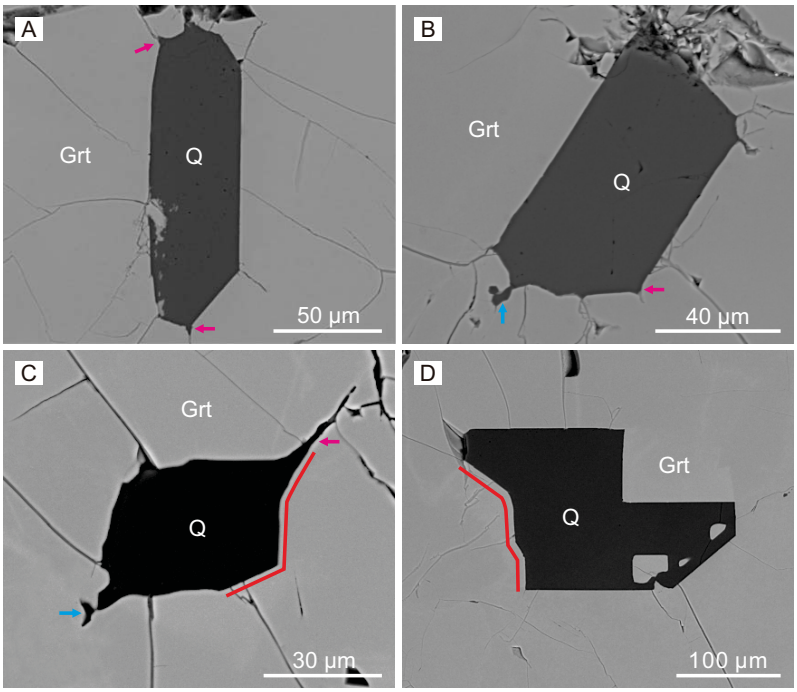

This is a preprint, the final version is subject to change, of the American Mineralogist (MSA)
Cite as Authors (Year) Title. American Mineralogist, in press.
DOI: https://doi.org/10.2138/am-2018-6395

Figure 3

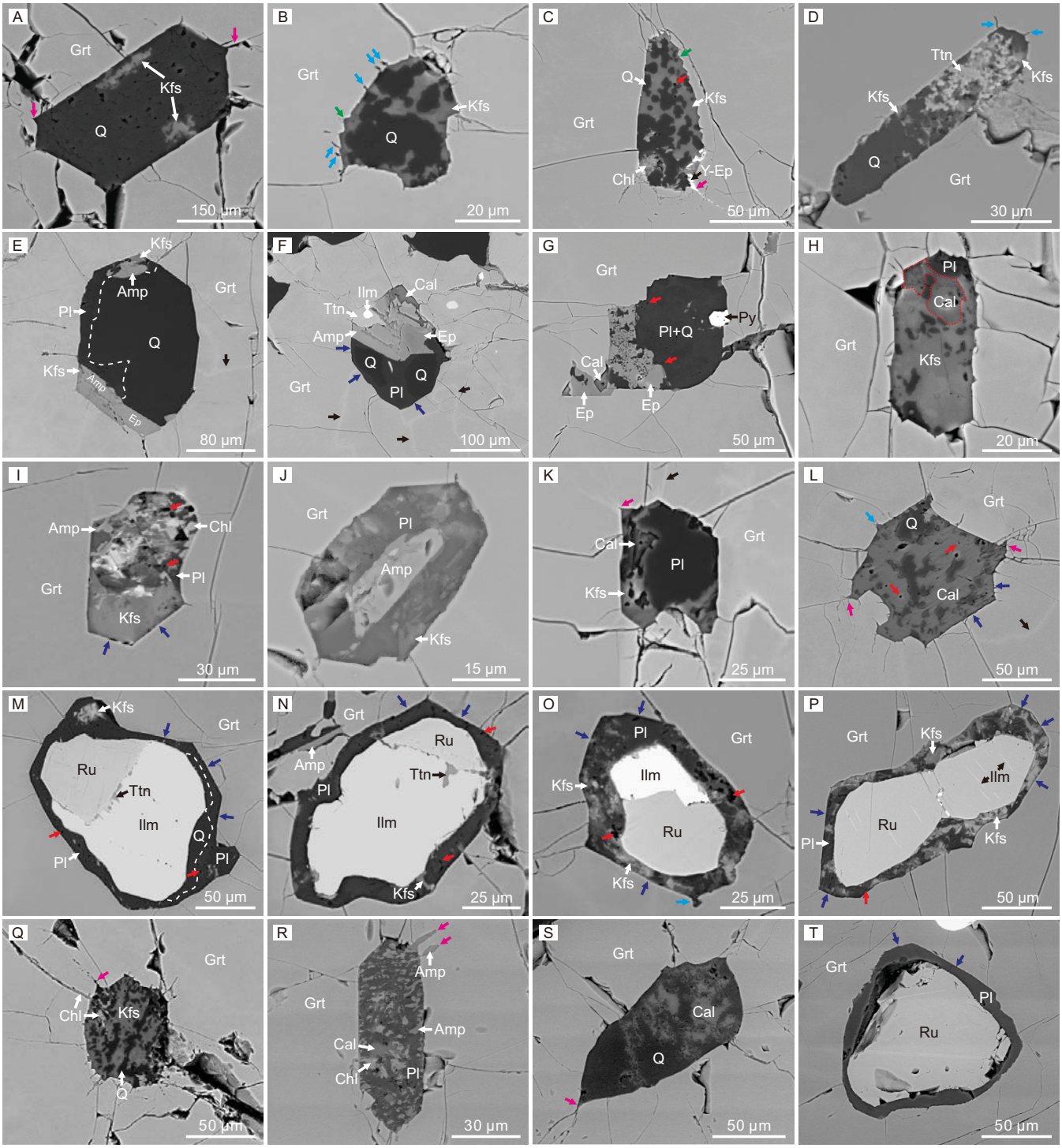

This is a preprint, the final version is subject to change, of the American Mineralogist (MSA)
Cite as Authors (Year) Title. American Mineralogist, in press.
DOI: https://doi.org/10.2138/am-2018-6395

Figure 4

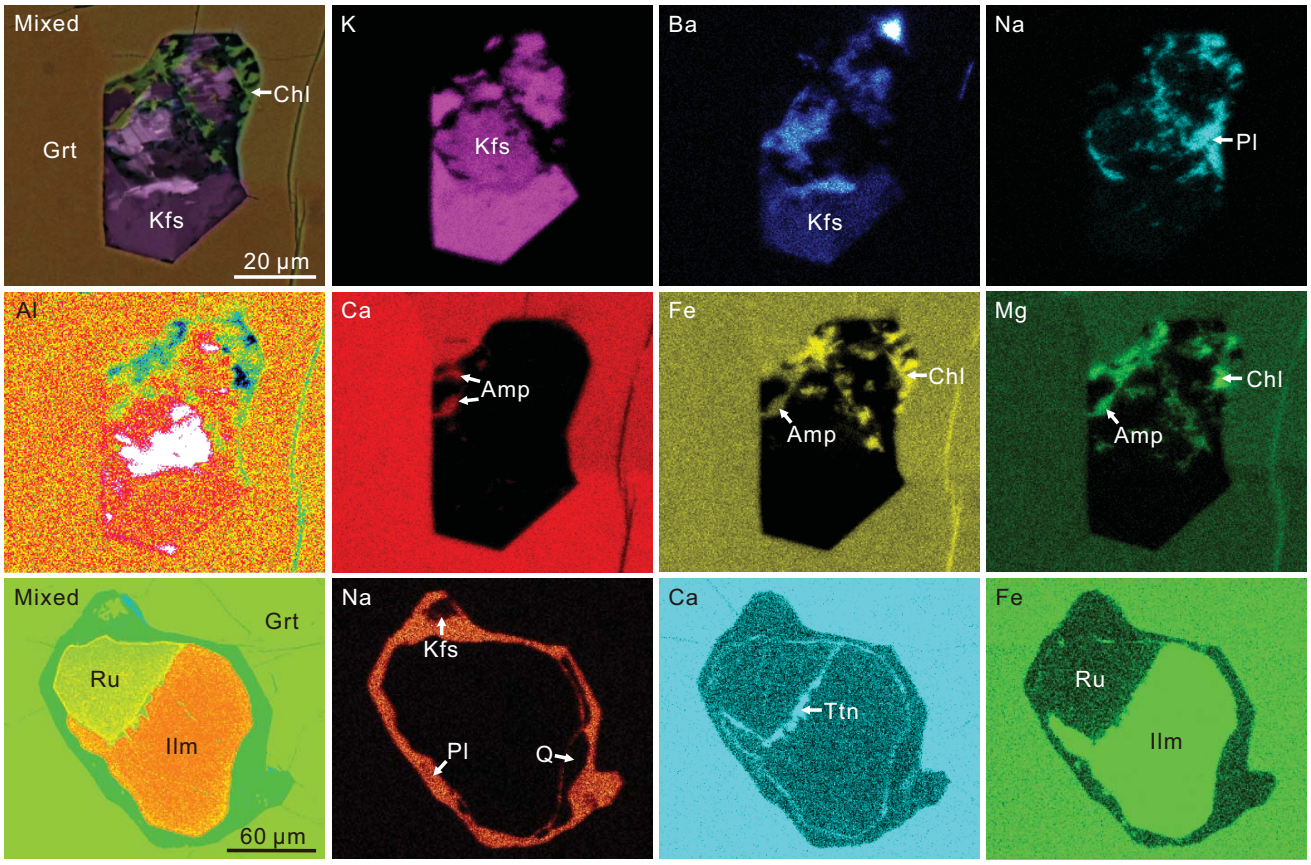

This is a preprint, the final version is subject to change, of the American Mineralogist (MSA)
Cite as Authors (Year) Title. American Mineralogist, in press.
DOI: https://doi.org/10.2138/am-2018-6395

Figure 5

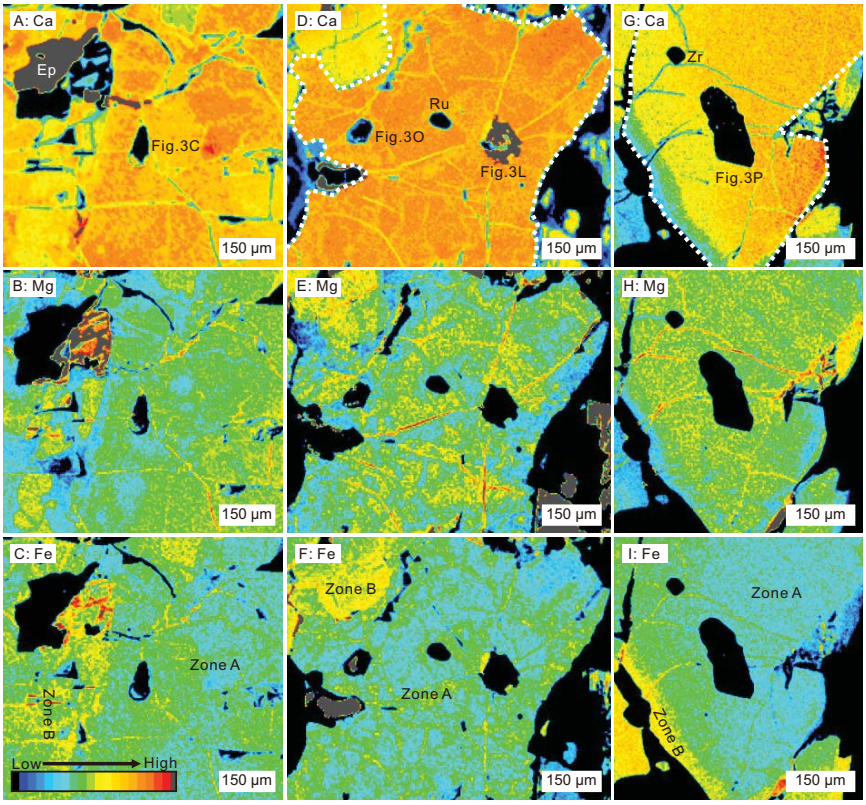

This is a preprint, the final version is subject to change, of the American Mineralogist (MSA)
Cite as Authors (Year) Title. American Mineralogist, in press.
DOI: https://doi.org/10.2138/am-2018-6395

Figure 6

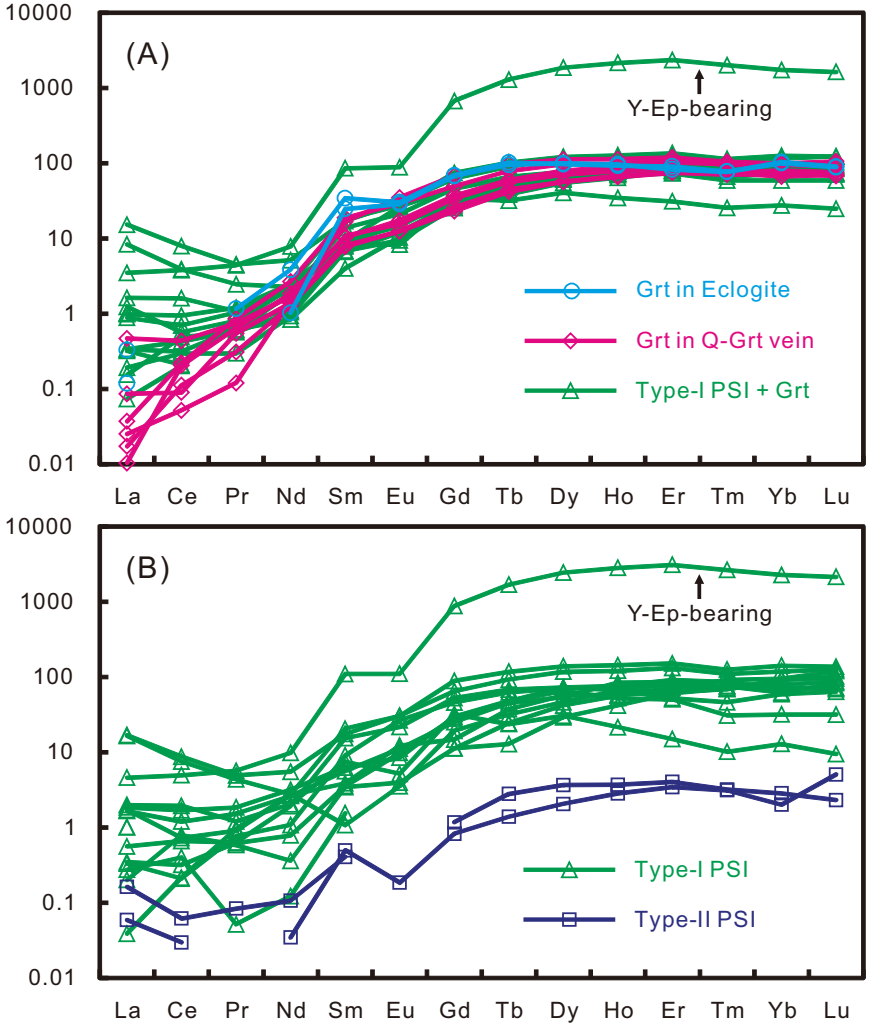

This is a preprint, the final version is subject to change, of the American Mineralogist (MSA)
Cite as Authors (Year) Title. American Mineralogist, in press.
DOI: https://doi.org/10.2138/am-2018-6395

Figure 7

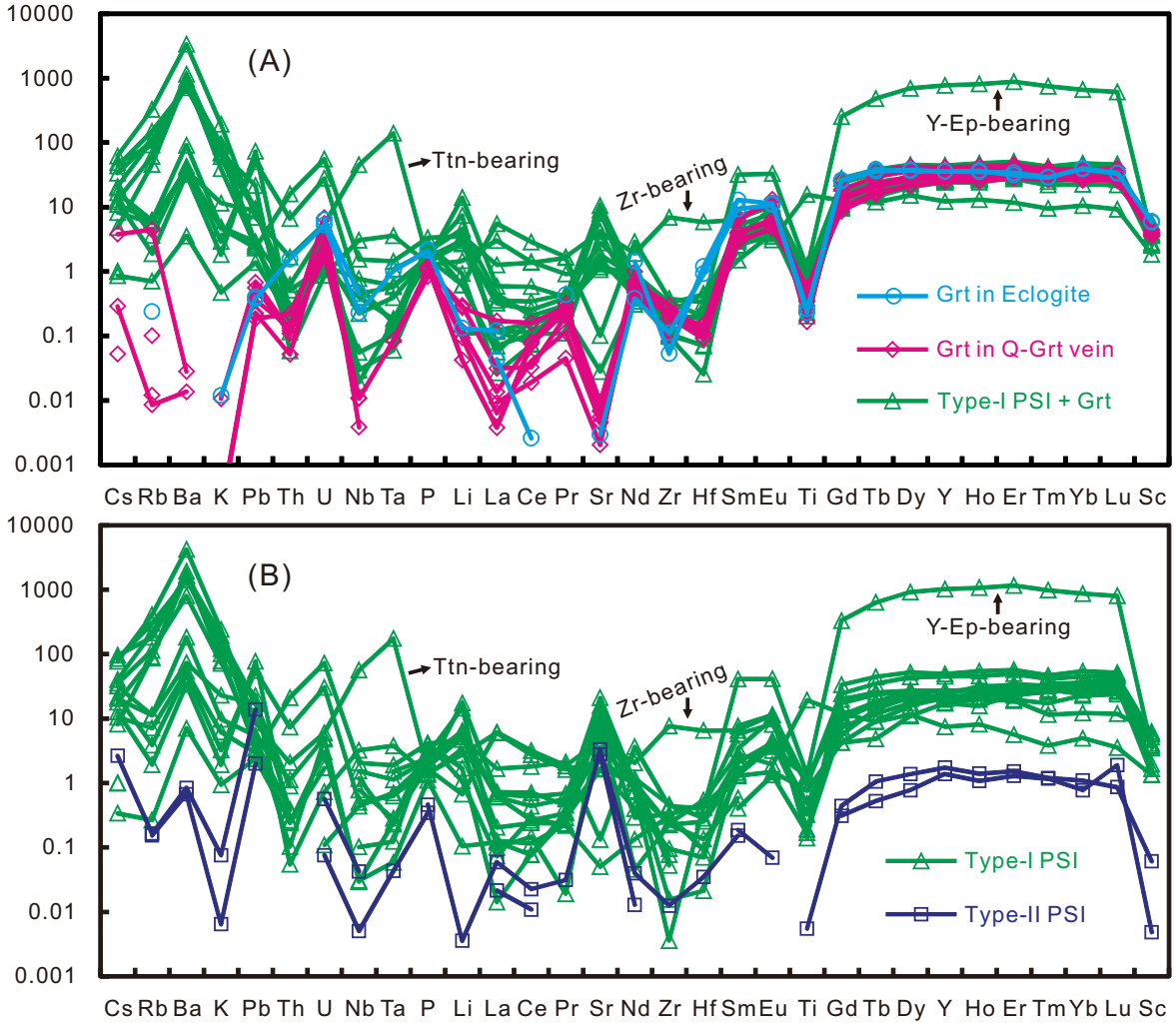

This is a preprint, the final version is subject to change, of the American Mineralogist (MSA)
Cite as Authors (Year) Title. American Mineralogist, in press.
DOI: https://doi.org/10.2138/am-2018-6395

Figure 8